



# HHS Public Access

Author manuscript

*ACS Appl Mater Interfaces*. Author manuscript; available in PMC 2023 August 03.

Published in final edited form as:

*ACS Appl Mater Interfaces*. 2022 August 03; 14(30): 34354–34364. doi:10.1021/acsami.2c06190.

## Renally Excretable Silver Telluride Nanoparticles as Contrast Agents for X-ray Imaging

**Lenitza M. Nieves,**

Department of Radiology, University of Pennsylvania, Philadelphia, Pennsylvania 19104, United States; Biochemistry and Molecular Biophysics Graduate Group, University of Pennsylvania, Philadelphia, Pennsylvania 19104, United States

**Yuxi C. Dong,**

Department of Radiology, University of Pennsylvania, Philadelphia, Pennsylvania 19104, United States; Department of Bioengineering, University of Pennsylvania, Philadelphia, Pennsylvania 19104, United States

**Derick N. Rosario-Berríos,**

Department of Radiology, University of Pennsylvania, Philadelphia, Pennsylvania 19104, United States; Biochemistry and Molecular Biophysics Graduate Group, University of Pennsylvania, Philadelphia, Pennsylvania 19104, United States

**Katherine Mossburg,**

Department of Radiology, University of Pennsylvania, Philadelphia, Pennsylvania 19104, United States; Department of Bioengineering, University of Pennsylvania, Philadelphia, Pennsylvania 19104, United States

**Jessica C. Hsu,**

Department of Radiology, University of Pennsylvania, Philadelphia, Pennsylvania 19104, United States; Department of Bioengineering, University of Pennsylvania, Philadelphia, Pennsylvania 19104, United States

**Gwendolyn M. Cramer,**

---

**Corresponding Author: David P. Cormode** – Department of Radiology, University of Pennsylvania, Philadelphia, Pennsylvania 19104, United States; Department of Bioengineering and Department of Cardiology, University of Pennsylvania, Philadelphia, Pennsylvania 19104, United States; david.cormode@penmedicine.upenn.edu.

Author Contributions

The project was designed by L.M.N., A.D.A.M., T.M.B., and D.P.C. Experiments were performed by L.M.N., Y.C.D., D.N.R.-B., J.C.H., and G.M.C. The manuscript was written by L.M.N. and D.P.C. All authors have contributed and approved the final version of the manuscript.

Supporting Information

The Supporting Information is available free of charge at <https://pubs.acs.org/doi/10.1021/acsami.2c06190>.

Additional experimental methods (4 nm GSH-Ag<sub>2</sub>Te NP synthesis, thermogravimetric analysis, and MTS assay), tables and result figures (FT-IR, thermogravimetric analysis, NP stability, micrographs from LIVE/DEAD and ROS generation assay, MTS assay, characterization, CT imaging, and biodistribution of 4 nm GSH-Ag<sub>2</sub>Te NPs, carcass biodistribution of 3 nm GSH-Ag<sub>2</sub>Te NPs), and a photograph of the 3 nm GSH-Ag<sub>2</sub>Te NPs in solution (PDF)

Complete contact information is available at: <https://pubs.acs.org/doi/10.1021/acsami.2c06190>

The authors declare the following competing financial interest(s): D. P. C. and A.D.A.M. are named as inventors on patent applications concerning silver-based contrast agents. They also hold stock in Daimroc Imaging, a company that is seeking to commercialize such agents.

The raw and processed data required to reproduce these findings are available from the corresponding author upon request.

Department of Radiation Oncology, University of Pennsylvania, Philadelphia, Pennsylvania 19104, United States

**Theresa M. Busch,**

Department of Radiation Oncology, University of Pennsylvania, Philadelphia, Pennsylvania 19104, United States

**Andrew D. A. Maidment,**

Department of Radiology, University of Pennsylvania, Philadelphia, Pennsylvania 19104, United States

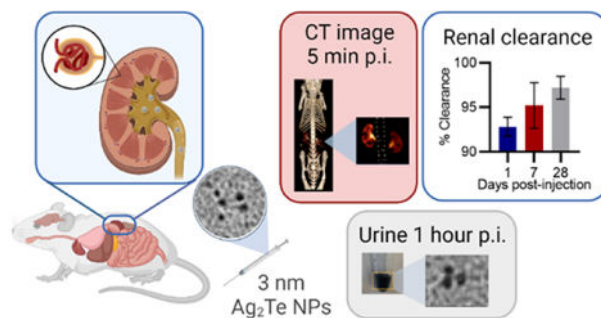
**David P. Cormode**

Department of Radiology, University of Pennsylvania, Philadelphia, Pennsylvania 19104, United States; Department of Bioengineering and Department of Cardiology, University of Pennsylvania, Philadelphia, Pennsylvania 19104, United States

## Abstract

The use of nanoparticles in the biomedical field has gained much attention due to their applications in biomedical imaging, drug delivery, and therapeutics. Silver telluride nanoparticles ( $\text{Ag}_2\text{Te}$  NPs) have been recently shown to be highly effective computed tomography (CT) and dual-energy mammography contrast agents with good stability and biocompatibility, as well as to have potential for many other biomedical purposes. Despite their numerous advantageous properties for diagnosis and treatment of disease, the clinical translation of  $\text{Ag}_2\text{Te}$  NPs is dependent on achieving high levels of excretion, a limitation for many nanoparticle types. In this work, we have synthesized and characterized a library of  $\text{Ag}_2\text{Te}$  NPs and identified conditions that led to 3 nm core size and were renally excretable. We found that these nanoparticles have good biocompatibility, strong X-ray contrast generation, and rapid renal clearance. Our CT data suggest that renal elimination of nanoparticles occurred within 2 h of administration. Moreover, biodistribution data indicate that 93% of the injected dose (%ID) has been excreted from the main organs in 24 h, 95% ID in 7 days, and 97% ID in 28 days with no signs of acute toxicity in the tissues studied under histological analysis. To our knowledge, this renal clearance is the best reported for  $\text{Ag}_2\text{Te}$  NP, while being comparable to the highest renal clearance reported for any type of nanoparticle. Together, the results herein presented suggest the use of GSH- $\text{Ag}_2\text{Te}$  NPs as an X-ray contrast agent with the potential to be clinically translated in the future.

## Graphical Abstract



## Keywords

silver telluride; renal clearance; nanoparticles; contrast agents; computed tomography

---

## INTRODUCTION

Inorganic nanoparticles serve many important functions in biomedical applications such as bioimaging, drug delivery, biosensors, and photothermal and photodynamic therapy for multiple diseases.<sup>1-4</sup> Yet, their clinical translation has been scant to date and is limited to the Food and Drug Administration (FDA) approval of several iron oxide nanoparticles and CE Mark approval of hafnium oxide nanoparticles.<sup>5-7</sup> One of the most important needs for clinical translation is the in-depth evaluation of the *in vivo* fate of nanoparticles over time and their interaction with different host cells and tissues.<sup>8,9</sup> Of particular importance is their interaction with the mononuclear-phagocytic system (MPS) (previously described as the reticuloendothelial system). The macrophages in the MPS organs (e.g., liver and spleen) typically uptake nanoparticles with a hydrodynamic diameter larger than 6 nm.<sup>10</sup> Once engulfed by the MPS, clearance of the nanoparticles is extremely slow and thus the nanoparticles could remain in the host for an extended period leading to an increased risk of toxicity.<sup>9,10</sup>

Renally excretable nanoparticles reduce the long-term safety concerns associated with MPS nanoparticle uptake.<sup>11-14</sup> Renal clearance of nanoparticles takes advantage of the kidney's glomerular filtration system to rapidly eliminate the particles through the kidneys and urine, with minimal accumulation in the MPS.<sup>15</sup> To achieve this, nanoparticles are developed with a diameter below the glomerular filtration threshold of 5.5 nm while incorporating surface coatings that avoid serum protein adsorption.<sup>11,12</sup> Nanoparticles with high serum protein adsorption can be taken up by the macrophages in the MPS organs.<sup>16-18</sup> Thus, avoiding serum protein adsorption through zwitterionic coatings, for example, favors renal clearance.<sup>11,19</sup> Therefore, renally clearable nanoparticles would consist, preferably, of a sub-5 nm size with zwitterionic coating and would be rapidly eliminated with minimal interaction with MPS organs.

Silver chalcogenide nanoparticles ( $\text{Ag}_2\text{X}$  NP, X = S, Te, or Se) have excellent properties for use in multiple biomedical applications.<sup>20</sup> Some of these properties include (1) optical properties and strong X-ray attenuation, (2) ease of surface functionalization, and (3) ultralow solubility products ( $K_{\text{sp}} \text{Ag}_2\text{S} = 6 \times 10^{-50}$ ,  $K_{\text{sp}} \text{Ag}_2\text{Se} = 3 \times 10^{-65}$ , and  $K_{\text{sp}} \text{Ag}_2\text{Te} = 2 \times 10^{-72}$ ), which leads to broad biocompatibility.<sup>20,21</sup> In a previous study, we reported silver telluride nanoparticles ( $\text{Ag}_2\text{Te}$  NPs) with a 16 nm hydrodynamic diameter.<sup>22</sup> These  $\text{Ag}_2\text{Te}$  NPs were biocompatible *in vitro* and *in vivo*, even at the high dose of 250 mg/kg of body weight used, which is appropriate for X-ray imaging. Their biocompatibility at this high dose suggested their safe use in several biomedical applications and their potential for clinical translation. However, their large size led to their accumulation in the MPS organs (25.2% ID/g in spleen and 15.1% ID/g in liver), raising potential concerns about their long-term safety. The challenge, therefore, for clinical translation of these highly promising

nanoparticles is to devise syntheses that result in ultrasmall sizes to allow sufficient renal clearance and study their safety over time.

To facilitate the clinical translation of Ag<sub>2</sub>Te NPs, we present the development of sub-5 nm Ag<sub>2</sub>Te NPs. To achieve this, we tested several chemical reactions with varying reaction times and different coatings. The optimal synthesis was achieved using 30 mM glutathione (GSH) as the Ag<sub>2</sub>Te NP coating. GSH is a zwitterionic molecule that has facilitated the renal clearance of other types of nanoparticles.<sup>11,23,24</sup> Here, we present the synthesis and characterization of the GSH-Ag<sub>2</sub>Te NPs, their X-ray contrast generation, *in vitro* and *in vivo* biocompatibility, and long-term safety. Most importantly, we evaluated whether the GSH-Ag<sub>2</sub>Te NPs met the requirements for renal excretion, where we found that 93% of the injected dose (%ID) was excreted from the main organs in 24 h, 95% in 7 days, and 97% in 28 days. To our knowledge, this renal clearance is markedly higher than the previously recorded values to date for Ag<sub>2</sub>Te and Ag<sub>2</sub>X NPs while being comparable to the highest renal clearance reported up to date for all types of nanoparticles.<sup>12,14,23,25–27</sup>

## MATERIALS

Silver nitrate (AgNO<sub>3</sub>) (ACS reagent, 99.0%) and L-glutathione reduced (GSH) (98.0%) were purchased from Sigma-Aldrich (St. Louis, MO). Sodium tellurite (Na<sub>2</sub>TeO<sub>3</sub>) (97%) and hydrazine hydrate, 80% (Hydrazine, 51%) (N<sub>2</sub>H<sub>4</sub>) were purchased from Alfa Aesar (Haverhill, MA) and Acros Organics (Thermo Fisher Scientific, NJ), respectively. Nitric acid (HNO<sub>3</sub>) (Certified ACS Plus) was purchased from Fisher Chemical (Thermo Fisher Scientific, Waltman, MA). Deionized water (DI) (Milli-Q at 18.2 MΩ cm) was used throughout the experiments.

## METHODS

### Nanoparticle Synthesis.

**General Ag<sub>2</sub>Te Nanoparticle Synthesis.**—Ag<sub>2</sub>Te NPs were synthesized by preparing an aqueous solution (9 mL volume), containing 10 mM AgNO<sub>3</sub>, 5 mM Na<sub>2</sub>TeO<sub>3</sub>, and the amount of coating described in Table S1. N<sub>2</sub>H<sub>4</sub> (1 mL) was then added to the solution. The reaction was allowed to proceed for the time and temperature described in Table S1 under constant magnetic stirring. Next, the NPs were washed thrice by centrifugation at 4000 rpm using 3 kDa molecular weight cutoff tubes. After the third wash, the particles were suspended in PBS and washed again as described above. The particles were then concentrated to 1 mL, filtered using 20 nm filters, and then stored at 4 °C until further use.

**GSH-Coated 3 nm Silver Telluride Nanoparticles.**—3 nm Core, GSH-coated Ag<sub>2</sub>Te NPs were synthesized by first placing an aqueous solution (9 mL volume), containing 10 mM AgNO<sub>3</sub>, 5 mM Na<sub>2</sub>TeO<sub>3</sub>, and 30 mM GSH, in an ice bath. N<sub>2</sub>H<sub>4</sub> (1 mL) was then added to the solution. The reaction was allowed to proceed for 5 min under constant magnetic stirring. Next, the NPs were washed thrice by centrifugation at 4000 rpm using 3 kDa molecular weight cutoff tubes. After the third wash, the particles were suspended in PBS and washed again as described above. The particles were then concentrated to 1 mL, filtered using 20 nm filters, and then stored at 4 °C until further use.

## Nanoparticle Characterization.

**UV–Vis Spectrometry.**—The UV–vis spectra of the Ag<sub>2</sub>Te NPs were recorded using a Genesys 150 UV/Vis spectrophotometer (Thermo Scientific). In brief, 5  $\mu\text{L}$  of the concentrated GSH-Ag<sub>2</sub>Te NPs was diluted in 995  $\mu\text{L}$  of DI water.

**Transmission Electron Microscopy (TEM).**—TEM micrographs were obtained to measure the nanoparticle core size. For this, we used a Tecnai T12 electron microscope operated at 100 kV. To prepare the samples, 10  $\mu\text{L}$  of the nanoparticle solution at a concentration of 0.5 mg/mL were added to a carbon-coated copper grid with 200 mesh purchased from Electron Microscopy Sciences (Hatfield, PA). The samples were then allowed to dry onto the grid. The core diameter was measured using ImageJ (National Institutes of Health, Bethesda, MA).

**Energy-Dispersive X-ray Spectrometry (EDX).**—The samples were prepared similarly to those for TEM. In brief, 10  $\mu\text{L}$  of the sample was dried onto carbon-coated copper grids. Data were acquired at 15 kV using an FEI Quanta 600 field emission gun scanning electron microscope.

**X-ray Diffraction Spectrometry (XRD).**—XRD samples were prepared by drying the concentrated NP samples on a silica disk. The diffraction patterns of the samples were acquired using a Rigaku MiniFlex X-ray diffractometer operated at 45 kV, 30 mA, 1.5406° Cu K $\alpha$  radiation wavelength, 2° per minute scan rate, and 20–60° scan range.

**Fourier Transformation Infrared (FT-IR) Spectroscopy.**—To create the FT-IR sample pellets, approximately 25 mg of the sample was added to 100 mg of potassium bromide. The samples were then dried in an oven, pulverized using a mortar and pestle, and embedded in the sample holder for analysis using a Jasco FT/IR-480 plus spectrometer.

**Inductively Coupled Plasma Optical Emission Spectroscopy (ICP-OES).**—A Spectro Genesis ICP-OES was used to determine the concentrations of Ag and Te in the samples. For this, 1 mL of nitric acid was added to 10  $\mu\text{L}$  of concentrated NP solution. The samples were allowed to digest over at least 1 h followed by the addition of 8.99 mL of DI water.

## *In Vitro* Biocompatibility Assays.

**Cell Culture.**—Cell culture of liver (HepG2) and kidney (Renca) cells was performed as recommended by the supplier, ATCC (Manassas, VA). In brief, 5% CO<sub>2</sub> was used to culture these cells at a temperature of 37 °C. The recommended cell media for each cell line were supplemented with fetal bovine serum (FBS) (Corning, Tewksbury, MA) and penicillin–streptomycin (Thermo Fisher Scientific, Waltham, MA).

**LIVE/DEAD Staining.**—Cell viability studies using LIVE/DEAD staining were performed as described elsewhere.<sup>22,28</sup> In brief, 80,000 cells were plated on 35 mm round-bottom dishes 24 h prior to the experiment. After 24 h, the cell media was removed and fresh medium (0 mg/mL control) or Ag<sub>2</sub>Te NPs at a concentration of 0.1, 0.25, 0.5, or 1 mg

of Ag/mL was added to the dishes. After 4 h, the treatment was removed and the cells were washed once with sterile PBS. A 400  $\mu$ L solution containing Calcein AM, Ethidium-1 homodimer, and Hoechst 33342 was added to the dishes and incubated for 20 min. After 20 min, the dishes were imaged using a Zeiss Axiovert fluorescence microscope equipped with FTIC, Texas Red, and DAPI filters. Four phase images and four images per filter were acquired for each dish. An in-house-developed MATLAB code was used to determine the number of live and dead cells. The percentage of viable cells was determined by the ratio of live to dead cells. The data were then normalized to the control and are presented as a percent of control and as mean  $\pm$  standard deviation.

**ROS Generation Colorimetric Assay.**—ROS generation was determined using the general oxidative stress assay CM-H2DCFDA (Invitrogen by Thermo Fisher Scientific, MD). In brief, 10,000 cells were seeded in each well of a 96-well plate 24 h prior to the experiment. The cells were incubated for 4 h with either cell medium (control) or GSH-Ag<sub>2</sub>Te NPs at different concentrations (0.1, 0.25, 0.5, and 1 mg of Ag per mL). After 4 h of incubation, the cells were washed with sterile PBS and incubated with CM-H2DCFDA for 25 min. H<sub>2</sub>O<sub>2</sub> diluted to 0.3% was used as a positive control for the detection of oxidative stress. Fluorescence from these samples was read using a Tecan M1000 plate reader at an excitation wavelength of 492 and 527 nm emission wavelength. Data are presented as relative fluorescence units  $\pm$  standard deviation.

**DNA Damage Assay.**—DNA damage was assessed using an immunofluorescence staining protocol to detect  $\gamma$ H2AX, an early marker of DNA damage. For this, 15,000 cells were seeded in each well of an eight-well glass slide chamber 24 h prior to the study. 24 h later, the cells were incubated with either cell culture medium (0 mg/mL control) or treated, in triplicate, with NPs at a concentration of 0.25, 0.5, or 1 mg of Ag per mL for 4 h. The cells were fixed with 4% paraformaldehyde, blocked, and incubated at 4 °C overnight with Phospho-Histone H2AX antibody (Cell Signaling, Danvers, MA). As positive controls, the cells were irradiated with a dose of 6 Gy delivered by a Precision X-Rad 320IX Biological X-Ray Irradiator 30 min prior to fixation. After washing with PBS, the cells were incubated with an anti-rabbit AF 594 secondary antibody for 1 h. Following mounting with Vectashield antifade mounting media containing DAPI, the slides were imaged at 20 $\times$  using a Zeiss AxioObserver Z1 equipped with DAPI and RFP filters. ImageJ was used to analyze the fluorescence intensity of the RFP and DAPI images. The mean intensity ratio was determined by calculating the ratio of RFP and DAPI fluorescence intensities. Data are presented as the mean ratio of fluorescence intensity from control  $\pm$  standard deviation.

### ***In Vitro* Imaging.**

**Computed Tomography (CT) Phantom Imaging.**—CT phantom images were acquired as described elsewhere.<sup>12,22</sup> In brief, to prepare the phantom, triplicate solutions silver (AgNO<sub>3</sub>), tellurium (Na<sub>2</sub>TeO<sub>3</sub>), Ag<sub>2</sub>Te NPs, and iopamidol of concentrations ranging from 0 to 10 mg of the element of interest per mL were prepared in 300  $\mu$ L tubes and placed in a plastic holder. Tubes containing PBS were used as negative controls. The phantom was then covered in parafilm and submerged in 21 cm of water to simulate the human body thickness. The scans were acquired using a Siemens SOMATOM Force clinical CT scanner

using the following parameters: 80, 100, 120, and 140 kV tube voltages; 360 mAs tube current;  $37 \times 37 \text{ cm}^2$  field of view; 0.5 mm thickness; and a  $512 \times 512$  matrix. The obtained images were analyzed using OsirixMD. A region of interest (ROI) was drawn in the tubes, and the intensities were recorded. The attenuation rate for each sample was determined from the average of three slices. Data are presented as attenuation rate  $\pm$  standard deviation.

### ***In Vivo* Imaging.**

**Animal Model.**—All animal procedures were performed following the Public Health Service (PHS) Policy on Humane Care and Use of Laboratory Animals (Public Law 99-158) per the University of Pennsylvania Guidelines for Care and Use of Laboratory Animals and approved by the Institutional Animal Care and Use Committee (IACUC) of the University of Pennsylvania under protocol number 805593.

Female nude mice were selected as the model for the experiments herein presented. In each experiment, five mice were used per group. A dose of 250 mg of Ag per kg of body weight of  $\text{Ag}_2\text{Te}$  NPs diluted in saline was injected into the mice via the tail vein.

**Computed Tomography (CT) Imaging.**—*In vivo* CT imaging was performed using a MILabs (Utrecht, The Netherlands) micro-CT scanner. Scans were acquired pre-injection, 5, 30, 60, and 120 min post-injection. The imaging parameters used were the following: 50 kVp, 210  $\mu\text{A}$ , 75 ms exposure, 0.75-degree step, and 360-degree acquisition. The images were reconstructed using the following parameters: 100  $\mu\text{m}$  reconstruction with 150  $\mu\text{m}$  gaussian post-filter. The obtained scans were analyzed using OsirixMD. ROIs were drawn in each organ of interest, and the attenuation was recorded. The data are presented as the change in attenuation from pre-injection images  $\pm$  standard error of mean (SEM).

**Biodistribution.**—Five female nude mice were euthanized per group, using  $\text{CO}_2$  gas for 5 min at 24 h, 7 days, or 28 days post-injections. Organs, i.e., liver, spleen, kidneys, lungs, and heart, were collected, along with feces and blood. The weights of these organs and tissues were recorded. The mice organs/tissues were then digested in either 4 (lungs, heart, bladder, and blood) or 6 mL (liver, spleen, and kidneys) of nitric acid and placed overnight in an oven at 90 °C. The next day, the samples were diluted to a final volume of 10 mL using DI water. The silver and tellurium concentrations were determined using ICPOES. Biodistribution data are presented as mean %ID  $\pm$  SEM.

**Histology.**—Following mice euthanasia with  $\text{CO}_2$  gas, tissue from the major organs of the mice was collected and sliced, in chilled PBS, into slices 5 mm in thickness. The tissues were then immediately fixed in 10% buffered formalin overnight at 4 °C. The samples were then processed and stained with hematoxylin and eosin (H&E) by the Children's Hospital of Philadelphia Pathology Core.

**Statistical Analysis.**—All experiments were performed at least three times, independently. Data are presented as mean  $\pm$  standard deviation (SD) or standard error of mean (SEM), as specified in each graph. *P* values  $< 0.05$  were considered statistically significant. Unpaired *t*-tests were used to compare the different groups in the CT phantom data. One-way ANOVA with Tukey's comparison test was used to compare the different data

groups in the ROS generation, cell viability, DNA damage, *in vivo* CT, and biodistribution experiments. Statistical analysis was carried out using GraphPad Prism 9 software (San Diego, CA).

## RESULTS

### Synthesis and Characterization of GSH-Coated Ag<sub>2</sub>Te Nanoparticles.

We sought to find the reaction conditions that led to ultrasmall Ag<sub>2</sub>Te NPs (<5.5 nm renal clearance threshold) while maintaining good colloidal stability. To achieve this, we varied the following parameters: coating molecule used and its concentration, reaction time, and reaction temperature. These reactions are summarized in Table S1. Note that while several of the 3-mercaptopropionic acid (3-MPA)-coated formulations met the size requirements, they were not colloidally stable in PBS or PBS with FBS over time. Based on the desired properties, the reaction conditions that yielded the most stable, ultrasmall Ag<sub>2</sub>Te NPs are depicted in Figure 1A. In brief, a solution containing silver and tellurium precursors in combination with GSH and N<sub>2</sub>H<sub>4</sub>, as the capping and reducing agents, respectively, was prepared. This solution was stirred for 5 min in an ice bath. The resulting nanoparticles had a broad UV–vis spectrum with no prominent peaks, which is characteristic of Ag<sub>2</sub>Te NPs (Figure 1B), and a core diameter of  $3 \pm 1$  nm (Figure 1C).<sup>22,29</sup> To confirm the successful coating of the nanoparticles with GSH, the  $\zeta$ -potential of the GSH-Ag<sub>2</sub>Te NPs was recorded and is presented in the inset of Figure 1C. This  $\zeta$ -potential agrees with previous studies that have reported a slightly negative  $\zeta$ -potential in GSH-coated nanoparticles.<sup>30,31</sup> Moreover, to further confirm the nanoparticle composition and successful coating with GSH, the EDX spectrum of the GSH-Ag<sub>2</sub>Te NPs was recorded. Figure 1D shows the characteristic X-ray peaks for silver (Ag), tellurium (Te), and sulfur (S), imparted by the GSH coating. These peaks confirm the composition of the nanoparticles and the successful incorporation of GSH as the nanoparticle coating. Supplemental Figure 1 shows the FT-IR spectra of the NPs compared to pure GSH. In addition, to further confirm and quantify the GSH surface coating, we performed thermogravimetric analysis of GSH and GSH-Ag<sub>2</sub>Te NPs. The results are shown in Supplemental Figure 2. Most of the weight change in both samples occurred near 200 °C, the melting point for GSH. Moreover, the derivative of weight change confirms a similar trend between GSH-Ag<sub>2</sub>Te NPs and GSH. At the maximum temperature tested of 500 °C, the total mass loss in the GSH-Ag<sub>2</sub>Te NPs was 41%. We hypothesize that the weight change corresponds to GSH and organic matter loss and not NP decomposition since the melting point for Ag<sub>2</sub>Te is 955 °C, well above the studied temperature. These results further confirm the successful GSH coating on the NPs. The XRD spectrum (Figure 1E) reveals peaks at  $2\theta = 26$  and  $38^\circ$ , which, while broader due to the small size of nanoparticles, are in agreement with previous reports.<sup>32–34</sup>

Aside from the previously discussed characterization data, the stability of GSH-Ag<sub>2</sub>Te NPs in water, PBS, and PBS with 10% FBS after 48 h of incubation was studied through UV–vis spectroscopy due to its high sensitivity to changes in nanoparticle size, concentration, and aggregation.<sup>35</sup> The study was conducted for 48 h because of the expected rapid clearance of these NPs *in vivo*. The UV–vis spectra are presented in Supplemental Figure 3. These data

show no change in the UV–vis spectra of the samples compared to the initial incubation time (0 h) and thus show the stability of the nanoparticles in the different media over 48 h.

### **GSH-Ag<sub>2</sub>Te NPs Are Biocompatible with Kidney and Liver Cells.**

An important requirement to facilitate clinical translation is the biocompatibility of the nanoparticles with the host. As a marker for the biocompatibility of GSH-Ag<sub>2</sub>Te NPs *in vivo*, we performed *in vitro* studies in cells from two of the main organs where renally excretable nanoparticles have been shown to interact the most: kidney (Renca cells) and liver (HepG2 cells).<sup>12,36</sup> We examined three biocompatibility parameters that better predict *in vivo* biocompatibility.<sup>37</sup> We first studied cell viability, through LIVE/DEAD and MTS assay, after incubation of the cells with the GSH-Ag<sub>2</sub>Te NPs. For this, Renca (kidney) and HepG2 (liver) cells were incubated with different concentrations (0, 0.1, 0.25, 0.5, and 1 mg of Ag per mL) of GSH-Ag<sub>2</sub>Te for 4 h followed by LIVE/DEAD and MTS assay staining. Results from these assays are presented in Figure 2A and Supplemental Figures 4 and 5. As shown in these figures, both assays reveal that GSH-Ag<sub>2</sub>Te were biocompatible (not statistically significantly different from control) with both cell lines after 4 h of incubation with the GSH-Ag<sub>2</sub>Te NPs, even at the highest concentration (1 mg of Ag/mL). Of note, this concentration, while relevant to CT imaging, is much higher than those required by other biomedical applications such as fluorescence imaging, photothermal therapy, and photodynamic therapy where concentrations in the  $\mu\text{g}/\text{mL}$  dose range are used. These results could speak to the future translation of these particles to different biomedical applications. In addition, the results are in agreement with previous reports in Ag<sub>2</sub>Te NPs and other silver chalcogenide particles.<sup>12,20,22</sup>

Another important parameter to determine the biocompatibility of the GSH-Ag<sub>2</sub>Te NPs with different cell types studied herein was the generation of reactive oxygen species (ROS). High ROS generation has been proven to be a common toxicity issue in the nanoparticle field, which could limit or impede their clinical translation.<sup>38,39</sup> ROS generation leads to toxicity in cells due to oxidative stress and thus can cause damage to cell organelles (including the mitochondria), DNA, cell membranes, ion channels, and cell receptors.<sup>38,39</sup> Here, we studied the ROS generation of GSH-Ag<sub>2</sub>Te, at different concentrations, in the two above-mentioned cell lines after 4 h of nanoparticle incubation. H<sub>2</sub>O<sub>2</sub> was used as a positive control. Figure 2B shows the results from the ROS generation assay. From these results, no increase in ROS generation after incubation with different concentrations, even at the highest studied concentration (1 mg of Ag per mL), was observed. These results are in agreement with results from our previous studies.<sup>22</sup>

The third assay to study the biocompatibility of these nanoparticles was their effect on DNA damage. For this, the GSH-Ag<sub>2</sub>Te NPs were incubated for 4 h, at different concentrations (0, 0.25, 0.5, and 1 mg of Ag per mL) with the above-mentioned cell lines. After the 4 h incubation period, DNA double-strand breaks were detected by phospho-histone H2AX ( $\gamma\text{H2AX}$ ) immunofluorescence. Results from our study are presented in Figure 2C and Supplemental Figure 6. Here, we can observe that 0.5 mg of Ag per mL for Renca cells and 1.0 mg of Ag per mL for HepG2 cells of GSH-Ag<sub>2</sub>Te NPs result in increases of this marker. Although we see significant DNA damage at high GSH-Ag<sub>2</sub>Te concentrations, the

low ROS generation and viability results have led us to hypothesize that the observed DNA damages could be repaired by the cells, as it is common for cells to activate DNA repair mechanisms, or DNA damage response, to sustain genomic integrity after any potential threat.<sup>40</sup> In addition, the extensive *in vivo* clearance discussed below, observed in CT images as early as 5–30 min post-injections, suggests a low probability of reaching these high nanoparticle concentrations in the cells in an *in vivo* setting.

### ***In Vitro* CT Imaging of GSH-Ag<sub>2</sub>Te NPs Resulted in Strong X-ray Attenuation.**

To test the X-ray contrast generating properties of the GSH-Ag<sub>2</sub>Te NPs, a phantom containing solutions of varying concentrations of silver salt (AgNO<sub>3</sub>), tellurium salt (Na<sub>2</sub>TeO<sub>3</sub>), iodine (iopamidol, as a control), and the NPs was used. To better mimic the imaging parameters in human patients' abdominal cavities, the CT phantom was submerged in 21 cm of water.<sup>41</sup> In addition, the contrast generation of these samples was evaluated under several of the X-ray energies (80, 100, 120, and 140 kV) most commonly used in the clinics. A representative image of the different samples acquired using 80 kV is presented in Figure 3A. Quantification of the attenuation rate of the samples is presented in Figure 3B. We found a high attenuation rate for the GSH-Ag<sub>2</sub>Te samples, higher than that of silver and tellurium salts. The attenuation rate of the GSH-Ag<sub>2</sub>Te NPs is comparable to that of iopamidol, a commonly used CT contrast agent in clinics, and higher at some energies. These data are in agreement with our previous publication, where we observed a higher contrast generation of mPEG 5k-coated Ag<sub>2</sub>Te NP than the silver and tellurium salts as well as iopamidol.<sup>22</sup> These results highlight the potential use of Ag<sub>2</sub>Te NPs as X-ray imaging contrast agents. While the attenuation rate of Ag<sub>2</sub>Te NPs seems similar to that of iopamidol in CT, in a previous study using the same materials, we found that Ag<sub>2</sub>Te NPs have a higher contrast-to-noise ratio in other X-ray imaging modalities that operate at lower X-ray energies such as dual-energy mammography and is predicted to be beneficial in dual-energy CT. Moreover, while the X-ray attenuation rate of these NPs is lower than that of other materials such as gold- and lanthanide-based NPs, we predict that the contrast generation of GSH-Ag<sub>2</sub>Te NPs can be significantly higher in other X-ray imaging modalities such as dual-energy CT and dual-energy mammography (DEM).<sup>22,28,42,43</sup> Both of these X-ray imaging techniques could benefit from the K-edges of Ag and Te as they utilize lower X-ray energies than those employed by conventional CT.

### ***In Vivo* Imaging Shows Renal Clearance within 2 h Post-Injection.**

An important parameter in the advancement of clinical translation is the ability of nanoparticles to be sufficiently eliminated from the body in a “reasonable” amount of time, as stated by the FDA.<sup>11</sup> To test whether the GSH-Ag<sub>2</sub>Te NPs met this requirement, tail vein injections were carried out in female nude mice, at a dose of 250 mg of Ag per kg of body weight. CT scans were obtained pre-injection and at 5, 30, 60, and 120 min post-injection. Representative 3D reconstruction images of a mouse are presented in Figure 4A. As can be seen, shortly after injection (5 min), we observed high contrast in the kidneys, as shown by the detailed kidney structures observed in the images (yellow arrow and magnified inset), and the start of their accumulation in the bladder (yellow dashed circle). As time progresses, we observed a decrease in the NP accumulation in the kidneys and higher accumulation in the bladder. At 60 min, we observed a much lower contrast in the bladder since the mouse

had recently urinated, clearing most of the NPs. Additional contrast was observed in the bladder at 120 min as the nanoparticles remaining in the mouse were transported into the bladder to be eliminated. The change in attenuation (HU), from the pre-injection images, at the different time points in several organs of the mice was quantified and is shown in Figure 4B. These data show the highest change in attenuation in the bladder with a decrease in attenuation over time. These data support the renal clearance of the GSH-Ag<sub>2</sub>Te NPs over time.

We developed GSH-Ag<sub>2</sub>Te NPs of slightly larger core size (4 nm) to examine the renal clearance threshold of this type of nanoparticle. The synthesis and characterization of these nanoparticles are shown in Supplemental Figure 7. As shown in Supplemental Figure 8, these nanoparticles caused high CT contrast in the liver and spleen, whereas very little contrast was observed in the kidneys or bladder. These results highlight how a slight increase in the nanoparticle diameter can result in an increase in nanoparticle retention in the MPS organs, as seen in previous reports.<sup>11</sup>

### **Biodistribution Shows Clearance of 93% ID in 24 h.**

Given the data obtained in the previous section, we further investigated the long-term biodistribution of the nanoparticles after *in vivo* administration. For this, groups of mice were injected with the GSH-Ag<sub>2</sub>Te NPs, euthanized at 24 h, 7 days, or 28 days post-injection, and their organs were collected for analysis. Figure 5A shows the %ID accumulated in the different organs at the studied time points. Supplemental Figure 9 shows data of nanoparticle accumulation in other tissues, including the mice carcass. Together these data show about 7% ID NP accumulation in main organs, thus suggesting a 93% ID clearance from these organs in 24 h. To our knowledge, this is markedly the highest renal clearance reported in 24 h for this type of particles and one of the highest renal clearance rates overall for nanoparticles.<sup>14,44</sup> At 7 days post-injection, 95% ID clearance from the main organs was observed with a significant decrease in the nanoparticle accumulation in organs such as the spleen and kidneys compared to 24 h. Furthermore, 97.5% ID was cleared at 28 days post-injection with a significant decrease in the nanoparticle accumulation in the liver and spleen compared to 7 days post-injection. Thus, these results suggest further significant clearance when comparing the already low nanoparticle accumulation at 24 h post-injection and that at 28 days. This high clearance could, thus, improve the chances of clinical translation for GSH-Ag<sub>2</sub>Te NPs.

In addition to biodistribution, the mice urine was collected and TEM micrographs of the nanoparticles in the urine were analyzed. Figure 5B shows a representative photograph of the urine collected pre-injection where a typical yellow color is observed in the inset, and no nanoparticles were observed in TEM micrographs. Figure 5C shows a representative TEM micrograph of mice urine collected 1-h post-injection and a photograph of the urine in the inset. From the photograph, we observed dark-colored urine, where this color closely matches the GSH-Ag<sub>2</sub>Te NP solution, as shown in Supplemental Figure 10. The average core size of the NPs observed in TEM from the urine at 1-h post-injection was 2.6 nm ( $\pm 0.9$  nm), which is not significantly different from the core size of GSH-Ag<sub>2</sub>Te NPs before injection ( $3 \pm 1$  nm). Moreover, the urine collected 24 h post-injection exhibited a yellow

color close to that of pre-injection, as observed in the inset of Figure 5D. The representative TEM micrograph in Figure 5D shows a few scattered NPs. It is worth noting that very few NPs were observed at this time point. In addition, as with the 1-h post-injection, the core size of the NPs observed at 24 h ( $3.2 \pm 0.7$  nm) is not of a significantly different size from the NPs before injection ( $3.1 \pm 1.3$  nm). The core sizes of the NPs at different time points are summarized in the table in Figure 5E. Together these data suggest the intact excretion of the NP core.

### No Evident Toxicity Was Observed in the Mice after GSH-Ag<sub>2</sub>Te Administration.

To further evaluate the long-term *in vivo* biocompatibility of the 3 nm GSH-Ag<sub>2</sub>Te NPs, mice weight was recorded over time, in addition to performing histological analyses and blood chemistry toxicological assays. Figure 6A shows the weight of control mice (uninjected) and mice injected with GSH-Ag<sub>2</sub>Te over 28 days. As shown in this figure, no significant difference in the weight of the two mice groups was observed. Moreover, no additional differences were observed in the mice's physical characteristics or behavior between the groups over the 28-day study period. For serum chemistry toxicology, blood was collected at 24 h, 7 days, and 28 days post-injection. The results from the toxicology panel are presented in Figure 6B–D. The high AST values shown in Figure 6B could be a result of hemolysis in the sample collection process. High levels of hemolysis have been shown to increase the AST values in some species by up to 50%.<sup>45</sup> These results show no statistically significant difference in the studied enzymes and marker levels in the serum of mice injected with GSH-Ag<sub>2</sub>Te at the various time points post-injection compared to control, thus suggesting no significant changes in the normal liver and kidney function of the mice at the various times post-injection compared to the control mice. For histological analysis, tissue from the main organs (i.e., heart, liver, spleen, kidneys, and lungs) was collected from mice at 24 h, 7 days, and 28 days post-injection. This tissue was then subjected to hematoxylin and eosin (H&E) staining. Mice injected with saline were used as controls. Figure 6E shows representative tissue slides from mice injected with saline or GSH-Ag<sub>2</sub>Te NPs at 1 day, 7 days, and 28 days post-injection. From these data, we observed no evident changes in the tissues of mice injected with GSH-Ag<sub>2</sub>Te at different time points compared to the control tissue. Together the histology and serum chemistry panels suggest that no signs of toxicity were further observed in the mice even after longer-term exposure (28 days) to the nanoparticles.

## DISCUSSION

Herein, we have developed an aqueous synthesis yielding 3 nm Ag<sub>2</sub>Te NPs using GSH as coating. This small core size of the GSH-Ag<sub>2</sub>Te NPs allows for their rapid excretion. In addition, the biocompatibility of the GSH-Ag<sub>2</sub>Te NPs is very good and is comparable to that of larger PEG-coated Ag<sub>2</sub>Te NPs previously developed by our group and other sub-5 nm silver chalcogenide NPs.<sup>12,22</sup> Their biocompatibility, even at high concentrations, speaks to the potential application of the NPs in different biomedical areas. Moreover, we herein report a renal clearance efficiency value (93% ID) comparable to the highest 24 h clearance rate reported to date (95% ID) for any type of nanoparticle.<sup>26</sup> This clearance is also the highest reported for Ag<sub>2</sub>Te and other Ag<sub>2</sub>X NPs (~85% ID) at 24 h post-injection.<sup>12,25,26</sup>

The renal clearance at 24 h post-injection for most nanoparticles is only around 50% ID.<sup>14</sup> While other Ag<sub>2</sub>Te NPs have been developed to achieve renal clearance, they report a clearance value of ~25% ID/g albeit at a much lower dose (>100 times lower).<sup>25</sup> Previous studies have reported a higher clearance rate in particles injected at a lower dose, further emphasizing the significance of the nanoparticles presented herein and their clearance.<sup>46</sup> Other Ag<sub>2</sub>X NPs have been developed to achieve renal clearance.<sup>12,47</sup> Examples include those reported by Ge et al. and Hsu et al. where Ag<sub>2</sub>Se and Ag<sub>2</sub>S nanoparticles were developed with core sizes of 2 and 3 nm, respectively.<sup>12,47</sup> Both studies reported a renal clearance of ~85% ID.<sup>12,47</sup> Moreover, the rapid renal excretion (93% ID in 24 h) reported herein led to less NP accumulation in the body over time, as shown in our long-term biodistribution study where only 4.8% ID remained in the main organs of the mice after 7 days of injection and 2.5% ID after 28 days. This low NP accumulation could lead to a better safety profile and could thus facilitate its clinical translation process. This efficient renal clearance, being among the highest reported to date, and their strong evidence of biocompatibility, even at the high concentrations used, can facilitate their clinical translation for their use as X-ray contrast agents and in many other biomedical applications (e.g., photothermal therapy, photoacoustic imaging, and near-infrared fluorescence imaging).

While the biocompatibility and renal clearance of the GSH-Ag<sub>2</sub>Te NPs met our experimental goals, the CT contrast generated by these NPs was slightly lower than that previously reported by our group.<sup>22</sup> We hypothesize that this lower contrast observed in 3 nm Ag<sub>2</sub>Te NPs compared to the larger NPs is due to the incorporation of fewer tellurium atoms in the NP cores, as shown by the higher ratio of Ag to Te in the EDX data in Figure 1D. This could be due to the larger surface area characteristic of smaller nanoparticles with more sites being occupied by the sulfur atoms in the capping agents at the surface as opposed to Te.<sup>48,49</sup> Future experiments could include optimizing the ratio of Ag to Te to further increase the contrast generated by these NPs. Furthermore, we predict that the contrast generation of GSH-Ag<sub>2</sub>Te NPs can be significantly higher in other X-ray imaging modalities such as dual-energy CT and DEM, as shown in our previous study.<sup>22</sup> Both dual-energy CT and DEM utilize much lower X-ray energies than that of conventional CT, which more closely align with the K-edge of Ag and Te. In the case of DEM, a lack of contrast agents specifically designed for this imaging technique currently exists leading clinics to rely on iodinated contrast agents which do not have optimal contrast and could cause adverse reactions in some patients. Thus, the high contrast generation of GSH-Ag<sub>2</sub>Te along with its biocompatibility and rapid excretion can lead to their application as DEM-specific contrast agents for breast cancer screening.

While the data presented in this study are promising for the further use of GSH-Ag<sub>2</sub>Te NPs in different biomedical applications and their subsequent clinical translation, we recognize some of the limitations of this study. For example, the biocompatibility studied here is limited to the cell lines and mouse models used. A broader assessment of their biocompatibility and *in vivo* toxicology would be desired for further clinical translation. Moreover, our future experiments include exploring the imaging properties of these nanoparticles in a mouse tumor model, especially using DEM or dual-energy CT. In addition, we will explore different ligands as capping agents for the Ag<sub>2</sub>Te NPs and test whether they could lead to higher clearance while achieving high NP accumulation in the

tumor site. This would be particularly beneficial for the use of renally clearable Ag<sub>2</sub>Te NPs as a contrast agent for cancer detection.

## CONCLUSIONS

We have developed an aqueous synthesis and extensively characterized the resulting 3 nm GSH-coated Ag<sub>2</sub>Te NPs. These NPs have the potential to be used as an X-ray contrast agent. Their contrast generation in CT was comparable to, if not higher than, commercially available iodinated contrast agents. In addition, GSH-Ag<sub>2</sub>Te NPs were shown to be biocompatible with kidney and liver cell lines showing no effect on the cell viability and low ROS generation after 4 h of incubation. The GSH-Ag<sub>2</sub>Te NPs showed high contrast in the kidneys and bladder rapidly after injection (i.e., 5 min post-injection), with this contrast decreasing over time as the particles were cleared through the urine over 2 h post-injection. Moreover, our biodistribution results suggest clearance of around 93% ID from main organs after 24 h of injection, 95% ID after 7 days, and 97% ID after 28 days. These clearance rates are, to our knowledge, the highest reported to date for Ag<sub>2</sub>Te NPs and among the best for any nanoparticle type. Moreover, the high dose of nanoparticles used in this study (250 mg/kg) can highlight their potential use in other biomedical applications. Together, the excellent biocompatibility and efficient renal clearance of GSH-Ag<sub>2</sub>Te NPs show their potential to be used as an X-ray contrast agent among other applications with good prospects for clinical translation.

## Supplementary Material

Refer to Web version on PubMed Central for supplementary material.

## ACKNOWLEDGMENTS

This work was possible thanks to funding by the National Institutes of Health (R01-CA227142-02S1 to L.M.N. and R01-CA227142-02 to D.P.C.), and Brody Family Medical Trust Fund Fellowship to J.C.H. In addition, this work was carried out in part at the Singh Center for Nanotechnology, which is supported by the NSF National Nanotechnology Coordinated Infrastructure Program under grant NNCI-2025608. The authors thank the Electron Microscopy Resource Laboratory at the University of Pennsylvania, especially Sudheer Molugu and Biao Zuo for their support with the TEM micrographs. They also thank Eric Blankemeyer for his help with micro-CT images.

## REFERENCES

- (1). Jiao M; Zhang P; Meng J; Li Y; Liu C; Luo X; Gao M Recent Advancements in Biocompatible Inorganic Nanoparticles Towards Biomedical Applications. *Biomater. Sci* 2018, 6, 726–745. [PubMed: 29308496]
- (2). Han X; Xu K; Taratula O; Farsad K Applications of Nanoparticles in Biomedical Imaging. *Nanoscale* 2019, 11, 799–819. [PubMed: 30603750]
- (3). Bouché M; Hsu JC; Dong YC; Kim J; Taing K; Cormode DP Recent Advances in Molecular Imaging with Gold Nanoparticles. *Bioconjugate Chem.* 2020, 31, 303–314.
- (4). Hsu JC; Nieves LM; Betzer O; Sadan T; Noël PB; Popovtzer R; Cormode DP Nanoparticle Contrast Agents for X-Ray Imaging Applications. *Wiley Interdiscip. Rev.: Nanomed. Nanobiotechnol* 2020, 12, No. e1642. [PubMed: 32441050]
- (5). Shreffler JW; Pullan JE; Dailey KM; Mallik S; Brooks AE Overcoming Hurdles in Nanoparticle Clinical Translation: The Influence of Experimental Design and Surface Modification. *Int. J. Mol. Sci* 2019, 20, 6056.

- (6). Metselaar JM; Lammers T Challenges in Nanomedicine Clinical Translation. *Drug Delivery Transl. Res* 2020, 10, 721–725.
- (7). Anselmo AC; Mitragotri S Nanoparticles in the Clinic: An Update. *Bioeng. Transl. Med* 2019, 4, No. e10143. [PubMed: 31572799]
- (8). Hua S; de Matos MBC; Metselaar JM; Storm G Current Trends and Challenges in the Clinical Translation of Nanoparticulate Nanomedicines: Pathways for Translational Development and Commercialization. *Front. Pharmacol* 2018, 9, 790. [PubMed: 30065653]
- (9). Najahi-Missaoui W; Arnold RD; Cummings BS Safe Nanoparticles: Are We There Yet? *Int. J. Mol. Sci* 2021, 22, 385.
- (10). Zhang YN; Poon W; Tavares AJ; McGilvray ID; Chan WCW Nanoparticle-Liver Interactions: Cellular Uptake and Hepatobiliary Elimination. *J. Controlled Release* 2016, 240, 332–348.
- (11). Soo Choi H; Liu W; Misra P; Tanaka E; Zimmer JP; Itty Ipe B; Bawendi MG; Frangioni JV Renal Clearance of Quantum Dots. *Nat. Biotechnol* 2007, 25, 1165–1170. [PubMed: 17891134]
- (12). Hsu JC; Cruz ED; Lau KC; Bouché M; Kim J; Maidment AD; Cormode DP Renally Excretable and Size-Tunable Silver Sulfide Nanoparticles for Dual-Energy Mammography or Computed Tomography. *Chem. Mater* 2019, 31, 7845–7854. [PubMed: 33005070]
- (13). Yang G; Phua SZF; Bindra AK; Zhao Y Degradability and Clearance of Inorganic Nanoparticles for Biomedical Applications. *Adv. Mater* 2019, 31, No. 1805730.
- (14). Peng C; Huang Y; Zheng J Renal Clearable Nanocarriers: Overcoming the Physiological Barriers for Precise Drug Delivery and Clearance. *J. Controlled Release* 2020, 322, 64–80.
- (15). Xu J; Peng C; Yu M; Zheng J Renal Clearable Noble Metal Nanoparticles: Photoluminescence, Elimination, and Biomedical Applications. *Wiley Interdiscip. Rev.: Nanomed. Nanobiotechnol* 2017, 9, No. e1453.
- (16). Kokkinopoulou M; Simon J; Landfester K; Mailander V; Lieberwirth I Visualization of the Protein Corona: Towards a Biomolecular Understanding of Nanoparticle-Cell-Interactions. *Nanoscale* 2017, 9, 8858–8870. [PubMed: 28632260]
- (17). Ahsan SM; Rao CM; Ahmad MF Nanoparticle-Protein Interaction: The Significance and Role of Protein Corona. In *Advances in Experimental Medicine and Biology*; Springer, 2018; Vol. 1048, pp 175–198. [PubMed: 29453539]
- (18). Walkey CD; Olsen JB; Guo H; Emili A; Chan WC Nanoparticle Size and Surface Chemistry Determine Serum Protein Adsorption and Macrophage Uptake. *J. Am. Chem. Soc* 2012, 134, 2139–2147. [PubMed: 22191645]
- (19). Liu J; Yu M; Ning X; Zhou C; Yang S; Zheng J Pegylation and Zwitterionization: Pros and Cons in the Renal Clearance and Tumor Targeting of Near-IR-Emitting Gold Nanoparticles. *Angew. Chem., Int. Ed* 2013, 52, 12572–12576.
- (20). Nieves LM; Mossburg K; Hsu JC; Maidment ADA; Cormode DP Silver Chalcogenide Nanoparticles: A Review of Their Biomedical Applications. *Nanoscale* 2021, 13, 19306–19323. [PubMed: 34783806]
- (21). Buketov EA; Ugorets MZ; Pashinkin AS Solubility Product and Entropies of Sulphides, Selenides, and Tellurides. *Russ. J. Inorg. Chem* 1964, 9, 292–294.
- (22). Nieves LM; Hsu JC; Lau KC; Maidment ADA; Cormode DP Silver Telluride Nanoparticles as Biocompatible and Enhanced Contrast Agents for X-Ray Imaging: An in Vivo Breast Cancer Screening Study. *Nanoscale* 2021, 13, 163–174. [PubMed: 33325953]
- (23). Xie M; Xu Y; Huang J; Li Y; Wang L; Yang L; Mao H Going Even Smaller: Engineering Sub-5 nm Nanoparticles for Improved Delivery, Biocompatibility, and Functionality. *Wiley Interdiscip. Rev.: Nanomed. Nanobiotechnol* 2020, 12, No. e1644. [PubMed: 32432393]
- (24). Hsu JC; Du Y; Sengupta A; Dong YC; Mossburg KJ; Bouche M; Maidment ADA; Weljie AM; Cormode DP Effect of Nanoparticle Synthetic Conditions on Ligand Coating Integrity and Subsequent Nano-Biointeractions. *ACS Appl. Mater. Interfaces* 2021, 13, 58401–58410. [PubMed: 34846845]
- (25). Dong L; Li W; Yu L; Sun L; Chen Y; Hong G Ultrasmall Ag<sub>2</sub>Te Quantum Dots with Rapid Clearance for Amplified Computer Tomography Imaging and Augmented Photonic Tumor Hyperthermia. *ACS Appl. Mater. Interfaces* 2020, 12, 42558–42566. [PubMed: 32830482]

- (26). Zhou M; Li J; Liang S; Sood AK; Liang D; Li C Cus Nanodots with Ultrahigh Efficient Renal Clearance for Positron Emission Tomography Imaging and Image-Guided Photothermal Therapy. *ACS Nano* 2015, 9, 7085–7096. [PubMed: 26098195]
- (27). Yu M; Zheng J Clearance Pathways and Tumor Targeting of Imaging Nanoparticles. *ACS Nano* 2015, 9, 6655–6674. [PubMed: 26149184]
- (28). Hsu JC; Naha PC; Lau KC; Chhour P; Hastings R; Moon BF; Stein JM; Witschey WRT; McDonald ES; Maidment ADA; Cormode DP An All-in-One Nanoparticle (AION) Contrast Agent for Breast Cancer Screening with DEM-CT-MRI-NIRF Imaging. *Nanoscale* 2018, 10, 17236–17248. [PubMed: 30191237]
- (29). Yarema M; Pichler S; Sytnyk M; Seyrkammer R; Lechner RT; Fritz-Popovski G; Jarzab D; Szendrei K; Resel R; Korovyanko O; Loi MA; Paris O; Hesser G; Heiss W Infrared Emitting and Photoconducting Colloidal Silver Chalcogenide Nanocrystal Quantum Dots from a Silylamide-Promoted Synthesis. *ACS Nano* 2011, 5, 3758–3765. [PubMed: 21500803]
- (30). Aydemir D; Hashemkhani M; Durmusoglu EG; Acar HY; Ulusu NN A New Substrate for Glutathione Reductase: Glutathione Coated Ag<sub>2</sub>S Quantum Dots. *Talanta* 2019, 194, 501–506. [PubMed: 30609564]
- (31). Moaseri E; Bollinger JA; Chandalvaie B; Johnson L; Schroer J; Johnston KP; Truskett TM Reversible Self-Assembly of Glutathione-Coated Gold Nanoparticle Clusters Via Ph-Tunable Interactions. *Langmuir* 2017, 33, 12244–12253. [PubMed: 28985465]
- (32). Sahu A; Qi L; Kang MS; Deng D; Norris DJ Facile Synthesis of Silver Chalcogenide (Ag<sub>2</sub>E; E = Se, S, Te) Semiconductor Nanocrystals. *J. Am. Chem. Soc* 2011, 133, 6509–6512. [PubMed: 21486029]
- (33). Cadavid D; Ibáñez M; Shavel A; Durá OJ; de la Torre ML; Cabot A Organic Ligand Displacement by Metal Salts to Enhance Nanoparticle Functionality: Thermoelectric Properties of Ag<sub>2</sub>Te. *J. Mater. Chem. A* 2013, 1, 4864–4870.
- (34). Kumar N; Ray SS; Ngila JC Ionic Liquid-Assisted Synthesis of Ag/Ag<sub>2</sub>Te Nanocrystals Via a Hydrothermal Route for Enhanced Photocatalytic Performance. *New J. Chem* 2017, 41, 14618–14626.
- (35). Ray TR; Lettiere B; de Rutte J; Pennathur S Quantitative Characterization of the Colloidal Stability of Metallic Nanoparticles Using Uv-Vis Absorbance Spectroscopy. *Langmuir* 2015, 31, 3577–3586. [PubMed: 25730093]
- (36). Gong L; Wang Y; Liu J Bioapplications of Renal-Clearable Luminescent Metal Nanoparticles. *Biomater. Sci* 2017, 5, 1393–1406. [PubMed: 28484751]
- (37). Elsaesser A; Howard CV Toxicology of Nanoparticles. *Adv. Drug Delivery Rev* 2012, 64, 129–137.
- (38). Yang W; Wang L; Mettenbrink EM; DeAngelis PL; Wilhelm S Nanoparticle Toxicology. *Annu. Rev. Pharmacol. Toxicol* 2021, 61, 269–289. [PubMed: 32841092]
- (39). Abdal Dayem A; Hossain MK; Lee SB; Kim K; Saha SK; Yang GM; Choi HY; Cho SG The Role of Reactive Oxygen Species (ROS) in the Biological Activities of Metallic Nanoparticles. *Int. J. Mol. Sci* 2017, 18, 120.
- (40). Carusillo A; Mussolino C DNA Damage: From Threat to Treatment. *Cells* 2020, 9, 1665.
- (41). Li C; Harris M; Tsilimingras D; Liu SZ; Sheng Y; Liu X Sagittal Abdominal Diameter and Its Socioeconomic Correlates: Perspective of Sex Differences. *BMC Public Health* 2021, 21, 486. [PubMed: 33706753]
- (42). Naha PC; Lau KC; Hsu JC; Hajfathalian M; Mian S; Chhour P; Uppuluri L; McDonald ES; Maidment AD; Cormode DP Gold Silver Alloy Nanoparticles (GSAN): An Imaging Probe for Breast Cancer Screening with Dual-Energy Mammography or Computed Tomography. *Nanoscale* 2016, 8, 13740–13754. [PubMed: 27412458]
- (43). FitzGerald PF; Colborn RE; Edic PM; Lambert JW; Torres AS; Bonitatibus PJ Jr.; Yeh BM Ct Image Contrast of High-Z Elements: Phantom Imaging Studies and Clinical Implications. *Radiology* 2016, 278, 723–733. [PubMed: 26356064]
- (44). Zhang XD; Wu D; Shen X; Liu PX; Fan FY; Fan SJ In Vivo Renal Clearance, Biodistribution, Toxicity of Gold Nanoclusters. *Biomaterials* 2012, 33, 4628–4638. [PubMed: 22459191]

- (45). Knezevic CE; Ness MA; Tsang PHT; Tenney BJ; Marzinke MA Establishing Hemolysis and Lipemia Acceptance Thresholds for Clinical Chemistry Tests. *Clin. Chim. Acta* 2020, 510, 459–465. [PubMed: 32771484]
- (46). Javidi J; Haeri A; Nowroozi F; Dadashzadeh S Pharmacokinetics, Tissue Distribution and Excretion of Ag<sub>2</sub>S Quantum Dots in Mice and Rats: The Effects of Injection Dose, Particle Size and Surface Charge. *Pharm. Res* 2019, 36, 46. [PubMed: 30719585]
- (47). Ge XL; Huang B; Zhang ZL; Liu X; He M; Yu Z; Hu B; Cui R; Liang XJ; Pang DW Glucose-Functionalized near-Infrared Ag<sub>2</sub>Se Quantum Dots with Renal Excretion Ability for Long-Term in Vivo Tumor Imaging. *J. Mater. Chem. B* 2019, 7, 5782–5788. [PubMed: 31482937]
- (48). Zhang P; Sham TK X-Ray Studies of the Structure and Electronic Behavior of Alkanethiolate-Capped Gold Nanoparticles: The Interplay of Size and Surface Effects. *Phys. Rev. Lett* 2003, 90, No. 245502. [PubMed: 12857200]
- (49). Wilson OM; Knecht MR; Garcia-Martinez JC; Crooks RM Effect of Pd Nanoparticle Size on the Catalytic Hydrogenation of Allyl Alcohol. *J. Am. Chem. Soc* 2006, 128, 4510–4511. [PubMed: 16594653]

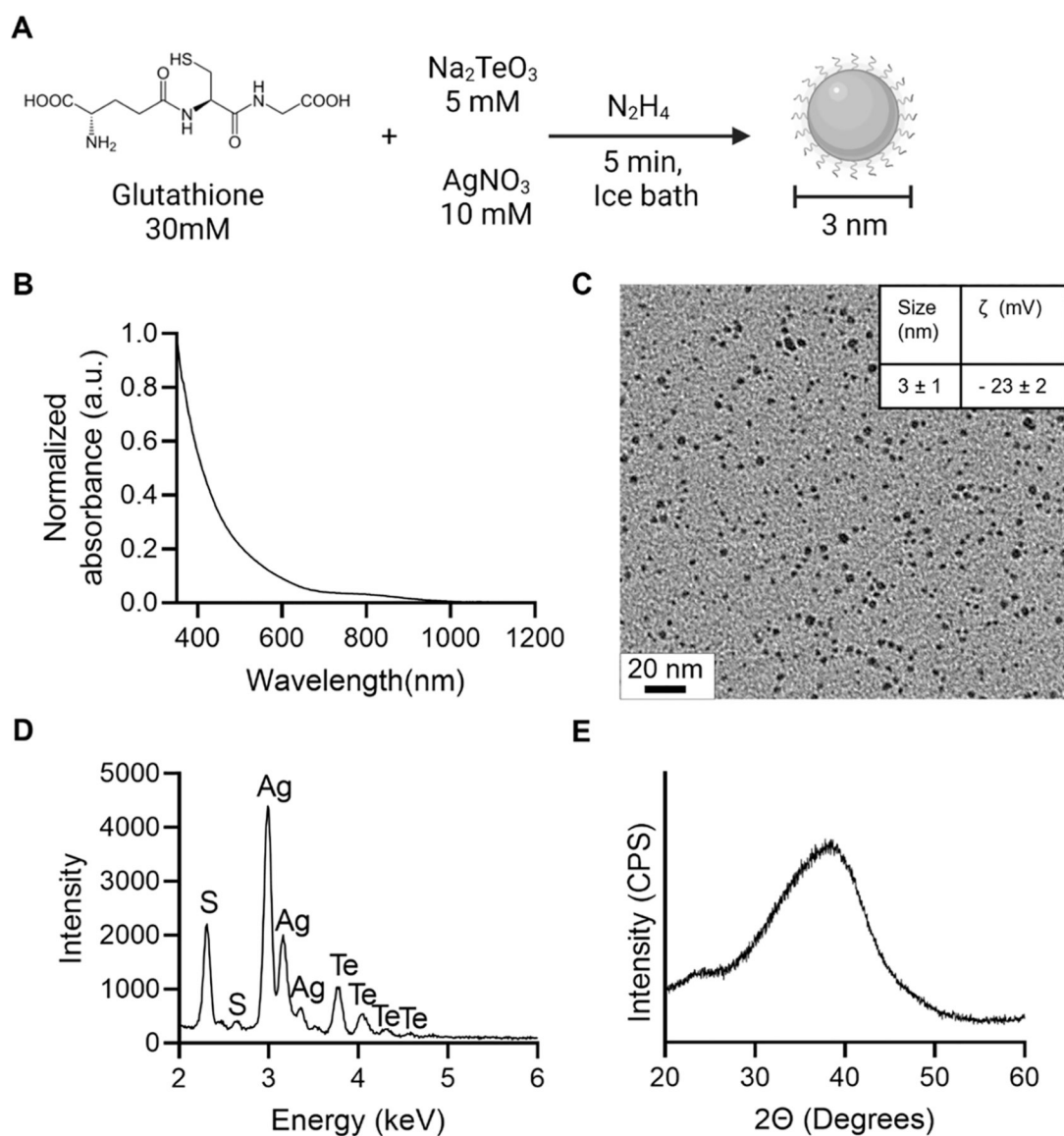


**Figure 1.** Nanoparticle synthesis schematic and characterization: (A) Nanoparticle synthesis schematic. (B) UV-vis spectrum of GSH-coated  $\text{Ag}_2\text{Te}$  NPs. (C) TEM micrograph of GSH-coated  $\text{Ag}_2\text{Te}$  NPs; the inset shows the core size and  $\zeta$ -potential data for GSH-coated  $\text{Ag}_2\text{Te}$  NPs. (D) EDX spectrum of GSH-coated  $\text{Ag}_2\text{Te}$  NPs. (E) XRD pattern of GSH-coated  $\text{Ag}_2\text{Te}$  NPs.

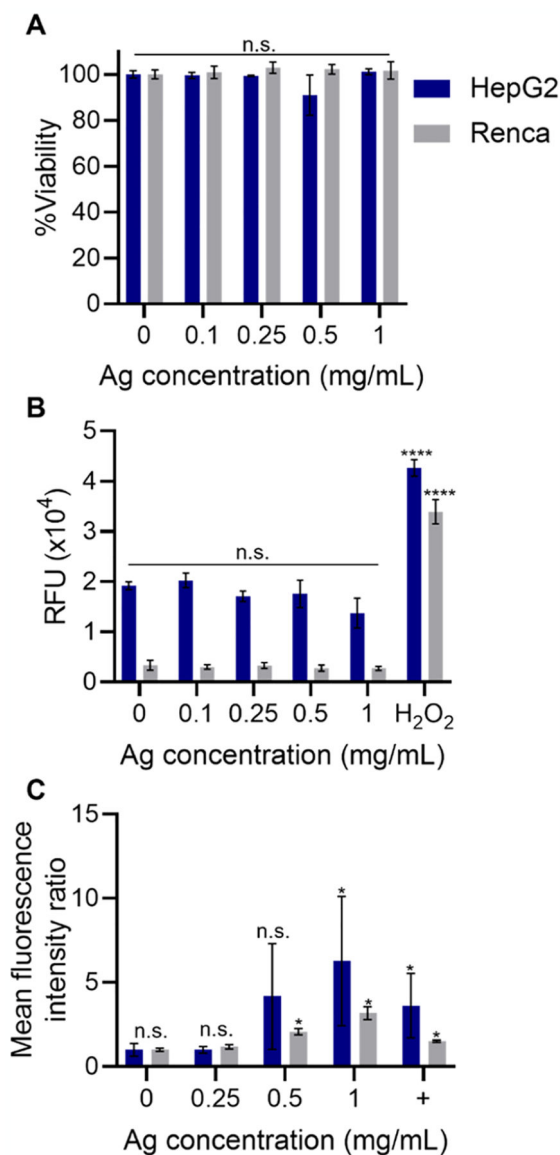


**Figure 2.**

*In vitro* biocompatibility assays. (A) Viability of kidney (Renca) and liver (HepG2) cells in gray and blue, respectively, (B) ROS generation of kidney cells and liver cells in gray and blue, respectively, and (C) immunofluorescence staining of  $\gamma$ H2AX in kidney and liver cells in gray and blue, respectively, after incubation with GSH-coated Ag<sub>2</sub>Te NPs at different Ag concentrations. In (C), + denotes positive controls (cells irradiated with a dose of 6 Gy 30 min prior to staining). Data are presented as mean  $\pm$  SD. Statistical significances are compared to the control. \* $p < 0.05$ . \*\*\*\* $p < 0.0001$ .  $n = 3$  per condition and cell line.

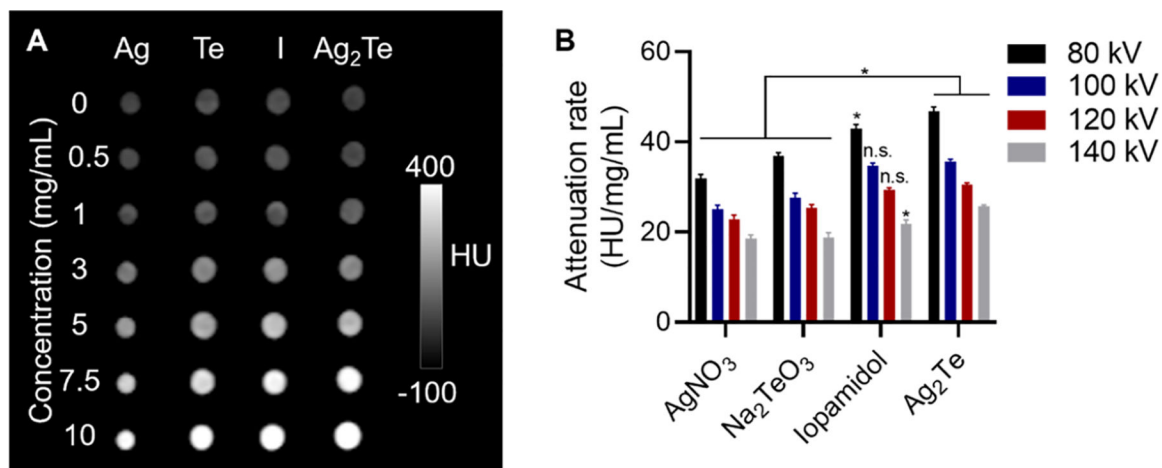


**Figure 3.**

*In vitro* CT imaging: (A) Representative CT images of AgNO<sub>3</sub> (Ag), Na<sub>2</sub>TeO<sub>3</sub> (Te), Iopamidol (I), and sub-5 nm GSH-coated Ag<sub>2</sub>Te NPs solutions at different concentrations (ranging from 0 to 10 mg/mL) at an X-ray tube voltage of 80 kV. (B) Quantification of the CT attenuation rate for the different solutions at varying X-ray tube voltages. Data are presented as mean ± SD. \**p* < 0.05, *n* = 3 per group.

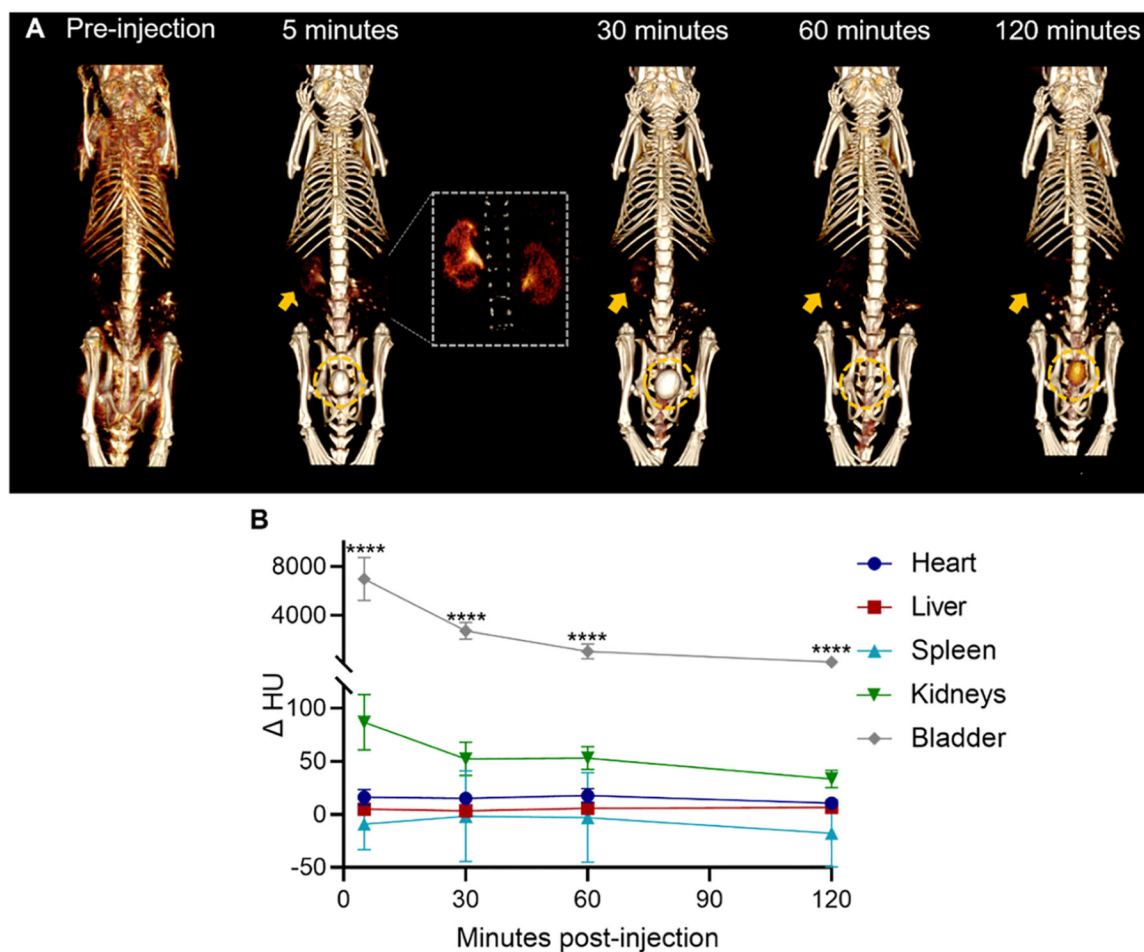


**Figure 4.**

*In vivo* CT imaging: (A) Representative 3D CT image reconstructions of 3 nm GSH-coated  $\text{Ag}_2\text{Te}$  NPs injected mice at pre- and 5, 30, 60, and 120 min post-injection. Window width (WW): 630 HU and window level (WL): 680 HU. Inset: 3D reconstruction magnification in the kidney region. WW: 429 HU and WL: 537 HU. (B) Quantification of the CT attenuation in the different organs of mice injected with GSH- $\text{Ag}_2\text{Te}$  NPs at different time points (5, 30, 60, 120 min post-injection).  $n = 5$  per group. Data are presented as mean  $\pm$  SEM. \*\*\*\* $p < 0.0001$ .

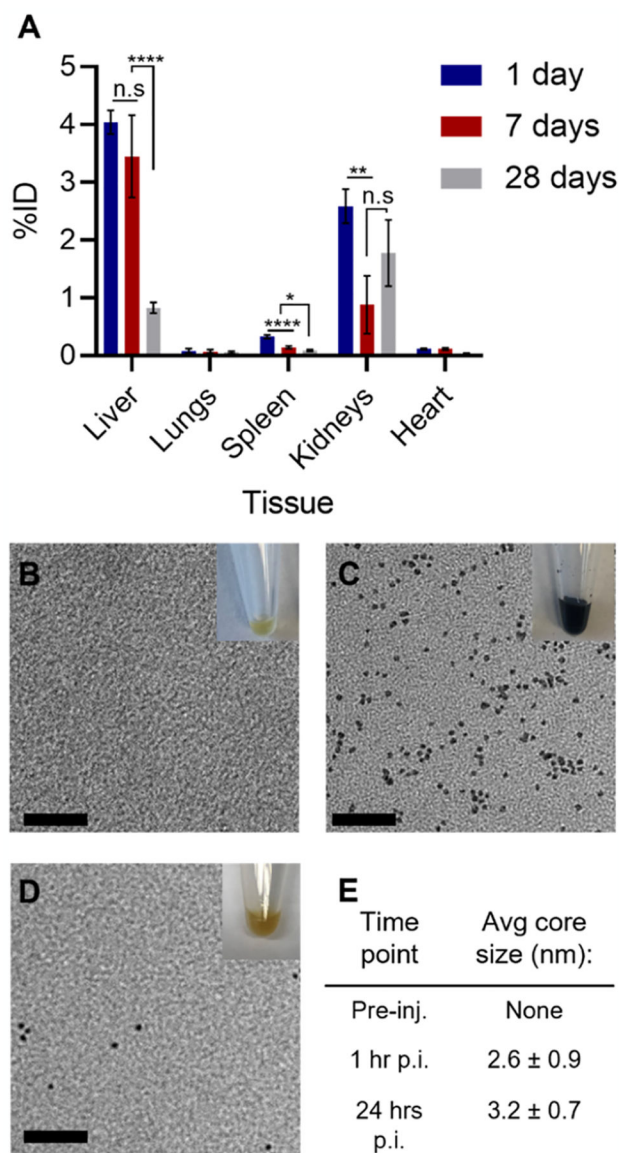


**Figure 5.** (A) Biodistribution at different times post-injection of sub-5 nm GSH-coated  $\text{Ag}_2\text{Te}$  NPs;  $n = 5$  per group. Data are presented as mean %ID  $\pm$  standard error of mean (SEM). Representative TEM micrograph of urine collected from the mice injected with sub-5 nm GSH-coated  $\text{Ag}_2\text{Te}$  NPs (B) pre-injection, (C) 60 min post-injection, and (D) 24 h post-injection. (E) Table showing the average core size of nanoparticle micrographs in (B–D). Inset: photograph of representative urine collected at the described time point. Scale bar represents 20 nm.

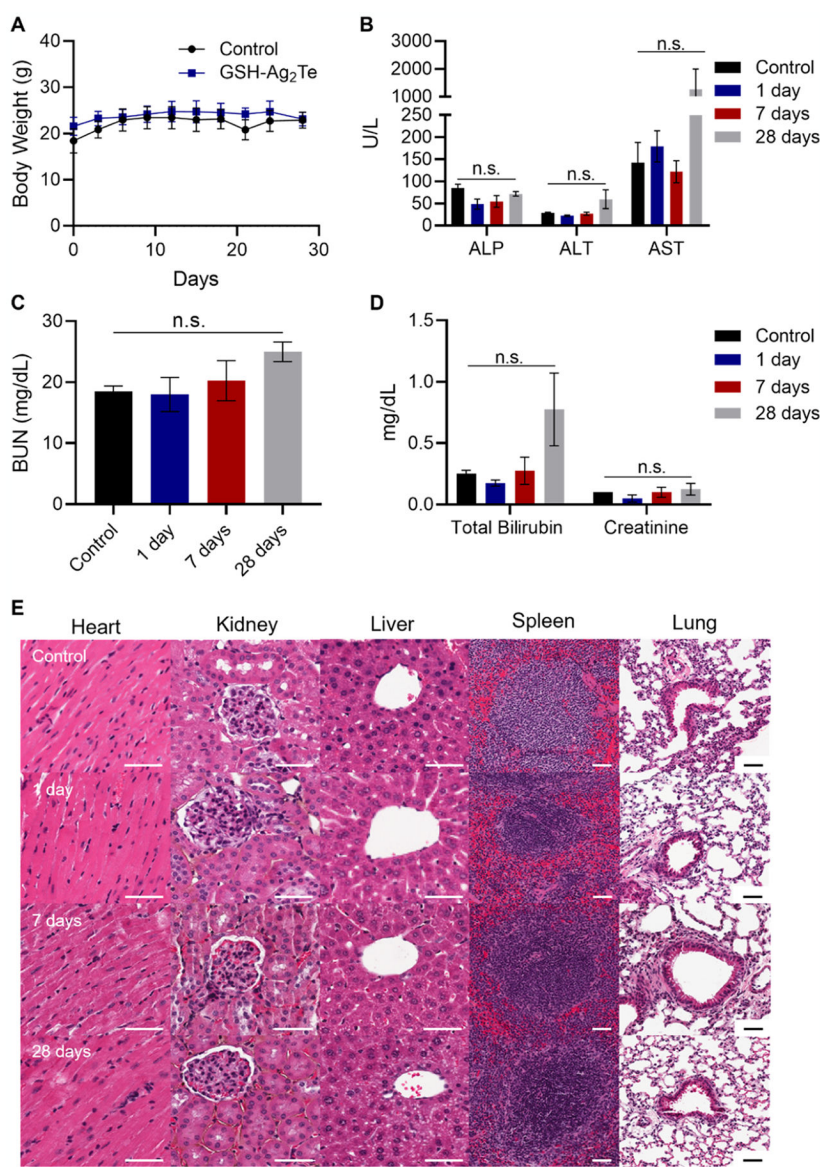


**Figure 6.** *In vivo* toxicology. (A) Body weight of control mice (uninjected) and GSH-Ag<sub>2</sub>Te-treated mice over 28 days. (B–D) Serum chemistry panels of mice injected with either PBS or GSH-Ag<sub>2</sub>Te at different times post-injection. Serum levels of (B) alkaline phosphatase (ALP), alanine aminotransferase (ALT), and aspartate aminotransferase (AST), (C) blood urea nitrogen (BUN), and (D) total bilirubin and creatinine in the different mice groups. Data are presented as mean ± SEM. (E) Representative histology (H&E staining) micrographs of mice organs after injection with either PBS or GSH-coated Ag<sub>2</sub>Te NPs at different times post-injection. *n* = 5 per group. Scale bar = 50 μm.